Journal of The Electrochemical Society, 2021 **168** 060555
1945-7111/2021/168(6)/060555/12/$40.00 © 2021 The Electrochemical Society ("ECS"). Published on behalf of ECS by IOP Publishing Limited

Investigation of the Impact of Flow of Vented Gas on Propagation of Thermal Runaway in a Li-Ion Battery Pack

Dhananjay Mishra,[1] Krishna Shah,[2,*] and Ankur Jain[1,z]

[1]*Mechanical and Aerospace Engineering Department, University of Texas at Arlington, Arlington, Texas, United States of America*
[2]*Mechanical Engineering Department, University of Texas at Austin, Austin, Texas, United States of America*

The venting of hot gases due to rupture of a Li-ion cell during thermal runaway may rapidly transfer thermal energy to neighboring cells in a battery pack and cause propagation of thermal runaway. While thermal runaway has been studied extensively through both measurements and simulations, there is a relative lack of research on the impact of the venting process on thermal runaway propagation. This work presents a non-linear thermal-fluidic simulation of supersonic turbulent flow of hot gases ejecting from a trigger cell and spreading to neighboring cells. Assuming isentropic flow, temperature and speed of the gas flow as functions of time are estimated based on past measurements. These data are used in simulations to determine the thermal impact of the venting process on neighboring cells. The impact of various geometrical parameters of the battery pack on the spreading of venting gases is investigated. Results indicate that cell-to-cell gap, overhead gap and the location of the vent hole on the cell body strongly influence the nature of propagation of thermal runaway to neighboring cells. This work develops a fundamental understanding of an important process during thermal runaway, and may help in the design and optimization of safe Li-ion battery packs for energy conversion and storage.
 [DOI: 10.1149/1945-7111/ac0a20]

Manuscript submitted April 15, 2021; revised manuscript received May 24, 2021. Published June 28, 2021.

List of symbols

b	hemispherical reflectivity
C_p	specific heat capacity ($Jkg^{-1}K^{-1}$)
f	shape factor
$\boldsymbol{g}$	acceleration due to gravity vector (ms^{-2})
k	thermal conductivity ($Wm^{-1}K^{-1}$)
L	length of the box (m)
p	pressure (Nm^{-2})
q''	heat flux (Wm^{-2})
q'''	volumetric heat generation rate (Wm^{-3})
R_u	universal gas constant ($Jmol^{-1}K^{-1}$)
T	temperature (K)
$\boldsymbol{V}$	velocity vector (ms^{-1})
α	thermal diffusivity (m^2s^{-1})
β	volumetric thermal expansion coefficient (K^{-1})
ε	hemispherical emissivity
γ	ratio of specific heats
ρ	density (kgm^{-3})
σ	Stefan-Boltzmann constant ($Wm^{-2}K^{-4}$)
μ	dynamic viscosity ($kgm^{-1}s^{-1}$)
ν	kinematic Viscosity (m^2s^{-1})
r,θ,z	Cylindrical coordinates
x,y,z	Cartesian coordinates

Thermal runaway in Li-ion cells is a key technological challenge that impacts the performance, safety and reliability of electrochemical energy conversion and storage devices.[1] Thermal runaway typically initiates when a cell is subjected to thermal, mechanical or electrical abuse conditions, such as high temperature, nail penetration or overcharging.[2] Decomposition of the Solid Electrolyte Interphase (SEI) layer occurs early in the thermal runaway process, which may generate sufficient heat to trigger decomposition reactions at the electrodes, eventually leading to decomposition and combustion of the electrolyte.[3] A cell undergoing thermal runaway may also rupture and release vent gases, which may contribute towards propagation of thermal runaway to neighboring cells in a battery pack.[2] Despite a large volume of past research, thermal runaway remains an active area of research, and methods for preventing, mitigating or predicting thermal runaway are of much interest.

In the context of large electrochemical energy conversion and storage systems, thermal runaway initiated in a single cell often propagates to neighboring cells, which eventually destroys the entire battery pack. Prevention of thermal runaway propagation is critical for limiting catastrophic failure of the entire battery pack. A number of studies have investigated the propagation of heat from one cell to the other in a large battery pack. Experimental measurements of thermal runaway propagation with a number of different cell chemistries and formats have been reported.[4–6] Accelerating Rate Calorimetry (ARC) is a commonly used experimental technique for measurement of thermal properties and heat generation rates.[7] Experimental analysis of thermal response of various Li-ion battery configurations to thermal abuse has been reported.[8] Numerical simulations have also been used to study a variety of aspects of thermal runaway propagation. For example, the role of thermal conduction through the interstitial material, as well as direct, surface-to-surface radiation between cells has been studied.[9] An optimal range of thermal conductivity has been identified.[9] The use of metal plates between cells and reducing the state of charge have been investigated for preventing propagation between cells.[10,11] A number of other cooling mechanisms have also been investigated for prevention of thermal runaway propagation, including phase change composite materials,[12,13] evaporative cooling,[14] liquid mist,[15] and aerosol insulation combined with a cooling plate.[16] The influence of different cell packing patterns on Li-ion thermal runaway propagation has also been investigated.[17] Investigation of thermal runaway in a battery pack initiated by mechanical nail penetration of one of the cells showed significant difference between pouch and cylindrical cells, and, for cylindrical cells, strong dependence on the electrical configuration of the battery pack.[18]

In addition to direct heat transfer between cells, gases venting out of the trigger cell after rupture may also play an important role in thermal runaway propagation. While the venting of hot gases from the trigger cell may momentarily cause cooling of the trigger cell due to evaporation and removal of hot material from the cell, the flow of vented gases outside the trigger cell causes advective transport of thermal energy to the surrounding cells. In addition, the vented gases may also combust outside the trigger cell, which generates even more heat.[2] The nature of venting during thermal runaway has been investigated in a number of papers. Coupled thermal and gas generation simulations based on finite-element

*Electrochemical Society Student Member.
[z]E-mail: jaina@uta.edu

technique have been reported for studying onset and evolution of thermal runaway venting in 18650 Li-ion cells.[19–21] The composition of vented gases is important for understanding post-venting events such as combustion and thermal advection, and has been reported in a number of papers. Measurements of total gas emission volumes, gas emission rates and amount of HF and CO_2 emissions during venting have been presented.[22] A key conclusion from this work was the large variability in venting time from a battery pack, ranging from 4 to 45 min depending on the chemistry of the underlying cells.[22] Differential Scanning Calorimetry (DSC) and gas chromatography measurements have been carried out to identify key species in the venting gas for a variety of cell chemistries and configurations.[23,24] Venting time of up to 30 s was reported for individual LFP cells.[25] It has been shown that temperature of the first detected exothermic reaction, maximum cell temperature, amount of vent gas and composition of vent gas depend strongly on SOC and the nature of abuse leading to thermal runaway.[25] Internal pressure change during venting of 18650 cells has been studied using computational fluid dynamics (CFD) simulations.[26] Cells at higher SOC were found to produce more heat and venting gas, resulting in higher internal pressure and subsequently a greater risk of side wall breaching.[26] A limited number of measurements of the temperature and speed of vent gases have also been reported. Specifically, burst pressure, vent opening area and discharge coefficient during choked-flow venting of 18650 Li-ion cell have been measured.[27] Experimentally validated finite-element simulations of the venting process have been used to determine Current Interrupt Device (CID) activation pressure and vent activation pressure at different ambient temperatures, showing that increasing temperature reduces vent activation pressure significantly.[28] This work also presented Computed Tomography (CT) scans of vent caps, providing useful insights into the vent release process in the case of overpressure. Based on this work, rupture of the cell on the top surface is expected when the safety valve is activated. However, if the safety valve malfunctions, or if there is weakening of the side wall due to mechanical impact, rupture may occur on the side wall.[29] Ejecta venting from side wall rupture may directly impinge on neighboring cells.

The advection of gases venting from the trigger cell into its surroundings, including in the gaps between neighboring cells, is a coupled heat and mass transfer problem, driven mainly by the gas pressure and speed at the vent hole. In this case, the temperature and velocity of escaping gases determines the amount of thermal energy transferred to the surroundings. While similar heat and mass transfer problems have been studied in other fields, such as dispersion of pollutants into the atmosphere[30] and oil recovery from sub-surface rocks,[31] similar work in the context of thermal runaway in Li-ion cells has not been reported in the past. While processes within the trigger cell leading up to venting, as well as the nature of vented gases have been widely studied, as summarized above, understanding the role of venting in the propagation of thermal runaway from one cell to the other is also very important, and will require a careful study of heat and mass transfer during and immediately after the venting event. A few interesting questions that such a study may help answer include whether advective heat transfer from the trigger cell to the battery pack via vent gas alone can cause thermal runaway propagation and how this would be impacted by the cell-to-cell gap, battery pack geometry and vent size and location on the trigger cell. Additionally, combined synergistic effects of venting and other heat transfer mechanisms on propagation may also be of interest.

This paper presents three-dimensional, non-linear numerical simulations of mass and heat transfer in a battery pack with hot gases venting out of a trigger cell. The constitutive energy, momentum and mass conservation equations along with appropriate boundary conditions are numerically solved. These simulations help characterize how the ejecta flow distributes thermal energy to the surrounding cells in the pack, and therefore, may contribute towards propagation of thermal runaway. Results indicate that the relative flow resistances encountered by ejecta flow for lateral transport and transport in the gap between cells play a key role in determining whether thermal runaway propagation occurs. The role of location of the vent hole is also shown to be an important determinant of propagation into neighboring cells. Results discussed here help understand an important mechanism underlying thermal runaway propagation in a battery pack. These results may help contribute towards the design of battery packs with improved thermal runaway safety and reliability.

Simulation Set up

Geometry.—Figure 1 shows top and side view schematics of the simulation geometry, which consists of a 5 by 5 array of uniformly arranged 18650 cells within an enclosed box. The volume between cells is occupied by air. In addition to the cell diameter, the two key geometrical parameters of this geometry are the cell-to-cell gap and the overhead gap, both of which are indicated in Fig. 1. The overhead gap is the clearance between the top of the cells and the battery pack enclosure. Hot ejecta is assumed to escape the trigger cell—cell 1 in the present simulations—from a 7 mm^2 circular vent hole and flow into the battery pack. Two locations of the vent hole—either on the top surface of the trigger cell, or on the curved surface with center positioned at 2.5 mm below the top surface and pointing towards cell 2—are considered in this work. These locations are indicated in Fig. 1. Rupture and venting from the top may occur if

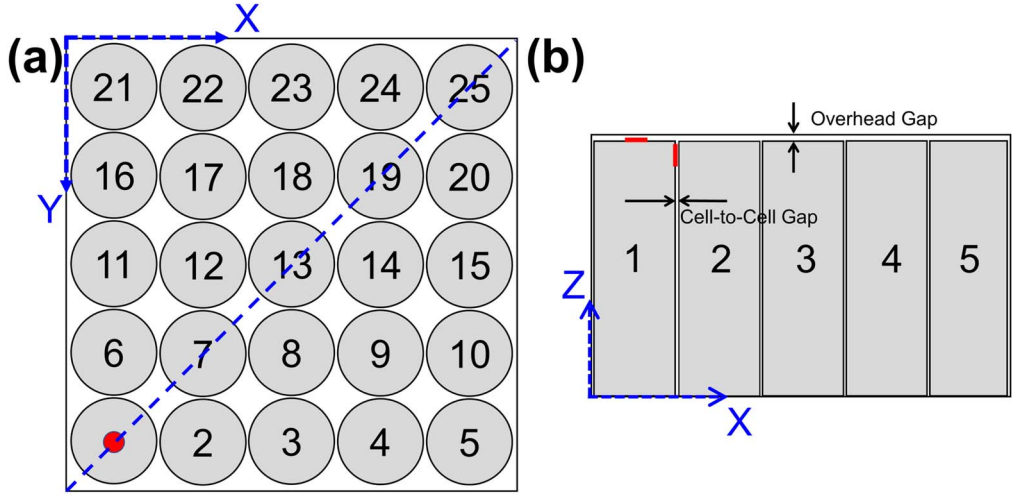

Figure 1. Schematic of 18650 Li-ion battery pack containing 25 cells: (a) Geometry of battery pack with trigger cell at position 1, including the diagonal symmetry plane. (b) Cross sectional view of the geometry in XZ plane.

the safety valve is released due to overpressure during thermal runaway. Rupture and venting from the side wall may occur if the safety valve malfunctions and/or if the side wall is weakened due to physical impact in case of mechanical abuse.[29] Side wall rupture is potentially more dangerous for thermal runaway propagation—and therefore important to study—as the ejecta might directly impinge on neighboring cells. The cells are assumed to be merely stored within the pack, and therefore, no charge/discharge of cells is considered. Secondary venting, i.e. venting from non-trigger cells to which thermal runaway propagates from the primary trigger cell is neglected.

Finite volume simulations are designed and carried out to account for fluid flow, and consequently heat transfer, induced by the ejecta escaping from the trigger cell. Temperature-dependent heat generation in the cells due to the various decomposition reactions is modeled using non-linear Arrhenius equations. Direct cell-to-cell heat transfer due to radiation is also accounted for. Thermal conduction between cells is ignored due to the much larger timescale for heat diffusion through materials such as electrical connectors compared to the advection timescale associated with the high speed flow. The presence of solid particles in the gas flow is ignored due to the potentially minor role played by the solid particles in cell-to-cell heat transfer, especially due to the high speed of the flow and relatively small fraction of solid particles in the flow. Heat generation due to reaction between vent gases and ambient air outside the cell is ignored due to the small time scale of the problem considered here. Governing equations for each phenomenon are described below in detail.

Governing equations.— *Mass, momentum and energy transport equations.*—Due to the high speed of venting gases, the vent flow is expected to be turbulent, necessitating detailed turbulence modeling for the flow. Amongst the multiple turbulence modeling techniques that have been proposed, the Spalart-Allmaras technique,[32] based on the Reynolds Average Navier–Stokes (RANS) method is used in this work. This technique has been used extensively in the past to model turbulent high-speed flows such as jets,[33] and shows good convergence without being memory-intensive. This technique also offers reduced computational effort as it needs to solve only one equation, unlike other solvers, which require more than one equation. In the Spalart-Allmaras technique, the mass conservation is given by the usual continuity equation, given by

$$\nabla.(\rho \mathbf{V}) = 0 \qquad [1]$$

The transport equation for any other variable a between two mesh elements i and j is given by

$$\frac{\partial(\rho.\mathrm{a})}{\partial \mathrm{t}} + \nabla_\mathrm{i}(\rho.\mathrm{a}.\mathrm{v}_\mathrm{i}) = \mathrm{G}_\mathrm{a} + \frac{1}{\sigma_\mathrm{a}}[\nabla_\mathrm{i}\{(\mu + \rho.\mathrm{a})\nabla_\mathrm{j}.\mathrm{a}\} + \mathrm{C}_{\mathrm{b}2}.\rho\nabla_j^2.\mathrm{a}] - \mathrm{Y}_\mathrm{a} + \mathrm{S}_\mathrm{a} \qquad [2]$$

Here, G_a is the production of turbulent kinematic viscosity, S_a is the source term and Y_a is the destruction of turbulent viscosity that occurs in the wall region due to wall blocking and viscous damping. C_{b2} and σ_a are constants with values of 0.622 and 2/3 respectively.[33] Details of the Spalart-Allmaras model are available in past work.[33]

Similarly, using Reynolds analogy to turbulent momentum transfer, turbulent heat transport equation for the turbulent flow can be written as

$$\frac{\partial(\rho.\mathrm{E})}{\partial \mathrm{t}} + \nabla_\mathrm{i}[\mathrm{v}_\mathrm{i}(\rho.\mathrm{E} + \mathrm{p})] = \nabla_\mathrm{j}\left[\left(\mathrm{k} + \frac{\mathrm{C}_\mathrm{p}\mu}{\mathrm{P}_\mathrm{r}}\right)\nabla_\mathrm{j}.\mathrm{T} + \mathrm{v}_\mathrm{i}(\tau_{\mathrm{ij}})_{\mathrm{eff}}\right] + \mathrm{S}_\mathrm{h} \qquad [3]$$

where k is thermal conductivity, E is total energy, S_h is the heat source term and $(\tau_{ij})_{eff}$ is the stress tensor.

Thermal conduction.—Heat transfer within each solid cell is governed by the thermal conduction equation

$$\frac{1}{r}\frac{\partial}{\partial \mathrm{r}}\left(\mathrm{k}_\mathrm{r}\mathrm{r}\frac{\partial \mathrm{T}}{\partial \mathrm{r}}\right) + \frac{\mathrm{k}_\theta}{\mathrm{r}^2}\frac{\partial^2 \mathrm{T}}{\partial \theta^2} + \mathrm{k}_\mathrm{z}\frac{\partial^2 \mathrm{T}}{\partial \mathrm{z}^2} + q''' = \rho \mathrm{c}_\mathrm{p}\frac{\partial \mathrm{T}}{\partial \mathrm{t}} \qquad [4]$$

where thermal conductivity within the cell is taken to be uniform, but orthotropic, and all properties are assumed to be independent of temperature.

Heat generation.—In addition to the advection of thermal energy due to the high-speed flow of the ejecta, heat is also generated within each cell. This strongly temperature-dependent heat generation occurs due to SEI decomposition, negative solvent reaction, positive solvent reaction and electrolyte decomposition.[34] The scenario considered here is that of storage of cells without charge/discharge, and therefore, the only heat generation within cells is due to decomposition reactions. A standard set of governing equations for these processes are used, and parameter values corresponding to $LiCoO_2$ cell chemistry are assumed. These equations and parameter values are easily available in past work,[35] and therefore, are not being included here. Heat generated in these decomposition reactions is implemented as a temperature-dependent volumetric heat generation term appearing in the energy conservation equation for the cells.

Each 18650 cell is modeled as a cylindrical orthotropic material, with values of 0.2, 32 and 32 $\mathrm{Wm^{-1}K^{-1}}$ in the radial, axial and circumferential directions, respectively, based on past measurements.[36] Density and heat capacity are taken to be 2280 $\mathrm{kgm^{-3}}$ and 715 $\mathrm{Jkg^{-1}K^{-1}}$, respectively, also based on past work.[34]

Radiative heat transfer.—The cells are expected to reach very high temperature during these simulations, both due to heat advected by the vent gases, as well as heat generation due to decomposition reactions associated with thermal runaway. As a result, radiation is expected to be an important mode of heat transfer and must be accounted for.

Radiation modeling between two surfaces is implemented using a surface-to-surface radiation model. Total energy flux leaving a surface comprises of irradiation flux from surroundings, known as reflected energy, and emitted energy by virtue of its own temperature. For any surface i, the amount of energy leaving the surface is:[37]

$$\mathrm{q}_{\mathrm{out,i}} = \varepsilon_\mathrm{i}\sigma\mathrm{T}_\mathrm{i}^4 + \mathrm{b}_\mathrm{i}\mathrm{q}_{\mathrm{in,i}} \qquad [5]$$

where ε_i and b_i are the emissivity and reflectivity, respectively, of the i^{th} surface, and σ is the Boltzmann constant. $q_{in,i}$ is the irradiation flux incident on the surface from the surroundings, which is given by the net sum of energy incident from all other surfaces based on the view factors f_{ji} as follows:

$$\mathrm{A}_\mathrm{i}{\cdot}\mathrm{q}_{\mathrm{in,i}} = \sum_{\mathrm{j}=1}^{\mathrm{N}} \mathrm{A}_\mathrm{j}{\cdot}\mathrm{q}_{\mathrm{out,j}}{\cdot}\mathrm{f}_{\mathrm{ji}} \qquad [6]$$

Therefore, total energy leaving the surface in Eq. 5 can be re-written as:

$$\mathrm{q}_{\mathrm{out,i}} = \varepsilon_\mathrm{i}{\cdot}\sigma\mathrm{T}_\mathrm{i}^4 + \mathrm{b}_\mathrm{i}{\cdot}\sum_{\mathrm{j}=1}^{\mathrm{N}} \mathrm{f}_{\mathrm{ij}}{\cdot}\mathrm{q}_{\mathrm{out,j}} \qquad [7]$$

Thus, the net radiation emitted from a surface comprises of emission from the surface and sum of radiation flux intercepted and reflected by virtue of other visible surfaces. In calculation of total radiation heat flux from a surface, view factors play a key role. For these simulations, view factors are computed using ray tracing method as described in a past study.[38] Radiation flux obtained is used as heat input for the energy equation of each cell. Each cell surface in the simulation geometry is considered as a diffuse gray surface with an

Table I. Key transport properties of the vent gas mixture for NCA[40] and LCO[41] cathode cells.

	$C_{p,avg}$ (kJkg^{-1}K^{-1})	$C_{v,avg}$ (kJkg^{-1}K^{-1})	γ	k_{avg} (Wm^{-1}K^{-1})	ν ($\times 10^{-5}$ m^{2}s^{-1})
NCA	3.386	2.642	1.280	0.05986	1.593
LCO	5.07	3.88	1.306	0.06154	1.382

emissivity of 0.1. Radiative properties of most practical surfaces are independent of direction and wavelength, which justifies the diffuse gray assumption. This assumption also results in time-efficient computation of radiative heat transfer at each timestep. Typical Li-ion cells have shiny metal casing, which justifies the low value of emissivity.

The governing equations listed above must be supplemented with appropriate boundary conditions. Boundary conditions for the vent through which the ejecta flows out of the trigger cell are deduced based on isentropic flow equations as described below. Whenever appropriate, diagonal symmetry is applied on the overall simulation geometry for efficient computation, resulting in adiabatic boundary condition on diagonal face of the box as shown in Fig. 1. Natural convective cooling to the ambient is modeled on the remaining four faces. In simulations involving an external opening on the battery pack, ambient pressure boundary condition is implemented on the external opening.

Isentropic flow equations.—This subsection describes the approach used for determining velocity and temperature of the vented ejecta as a function of time based on stagnation pressure and mass flow rate measurements.[27] The temperature and velocity values calculated based on this approach are used to specify boundary conditions on the outlet vent for the ejecta. This approach utilizes stagnation pressure measurements reported in the past for venting of similar Li-ion cells.[27] First, the Mach number of the ejecta can be obtained by inserting the experimental pressure measurements in the following relationship:[39]

$$\frac{p_0}{p} = \left(1 + \frac{\gamma - 1}{2} * Ma^2\right)^{\frac{\gamma}{\gamma-1}} \quad [8]$$

where the freestream pressure is considered to be constant at 1 atm. Mach number is then used, along with thermophysical properties of ejecta and mass flow rate measurements, to determine stagnation temperature T_0 as follows[39]

$$\frac{\dot{m}}{A} = \sqrt{\frac{\gamma}{R}} * \frac{p_0}{\sqrt{T_0}} * Ma\left(1 + \frac{\gamma - 1}{2} * Ma^2\right)^{\frac{\gamma+1}{2(\gamma-1)}} \quad [9]$$

Finally, the venting temperature is determined from T_0 by considering isentropic flow through the vent outlet, assuming the ejecta to be a perfect gas. Under these conditions, the venting temperature is related to stagnation temperature as follows:[39]

$$\frac{T_0}{T} = \left(1 + \left(\frac{\gamma - 1}{2}\right) * Ma^2\right) \quad [10]$$

Further, the acoustic speed is obtained from the following relationship:

$$a = \sqrt{\gamma RT} \quad [11]$$

Note that the Mach number is the ratio of flow speed to acoustic speed. Therefore, from the computed values of Mach number and acoustic speed as functions of time, the flow speed can be determined as a function of time.

All required thermophysical properties are calculated based on weighted average of gaseous components (CO_2, H_2, C_2H_4, CO, CH_4, C_3H_6, C_2H_5F) reported for Lithium Nickel Cobalt Aluminium Oxide (NCA)[40] and Lithium Cobalt Oxide (LCO)[41] type cathodes using Coolprop,[42] an open source fluid property database. The vent gas is assumed to be a calorically perfect gas. The three-coefficient Sutherland viscosity model is used to account for temperature dependent change in viscosity of the ejecta.[43] Key transport properties, including γ for the two cell types are summarized in Table I. It is found that the composition, and hence transport properties of the vent gas mixture is very close to each other for NCA and LCO cathode chemistries. Specifically, γ for the two cell types are within 2% of each other. The closeness of transport properties is likely because the gases in the vent are mainly organic, and, therefore, strongly dependent on the electrolyte and only weakly dependent on the cathode material.

Based on the isentropic flow analysis described above, fourth degree polynomial curve-fit expressions for transient velocity and temperature for the vent gas are determined to be

$$V(t) = -12.59t^4 - 73.387t^3 + 180.18t^2 + 20.66t + 218.76 \quad [12]$$

$$T(t) = 86.146t^4 - 345.78t^3 + 749.76t^2 - 153.27t + 361.82 \quad [13]$$

where t, T and V have units of s, K and ms^{-1}, respectively.

Figure 2 plots the vent velocity and temperature as functions of time based on the calculations outlined above for both NCA and LCO cell types. Data for the two cell types are very similar to each other due to very similar values of γ. This shows that there is negligible difference between venting characteristics between the two chemistries.

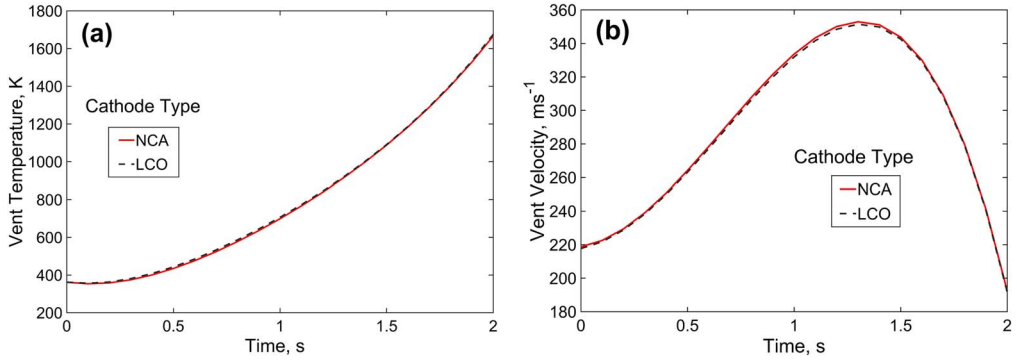

Figure 2. Temperature and velocity of venting gas as functions of time determined from the described calculations.

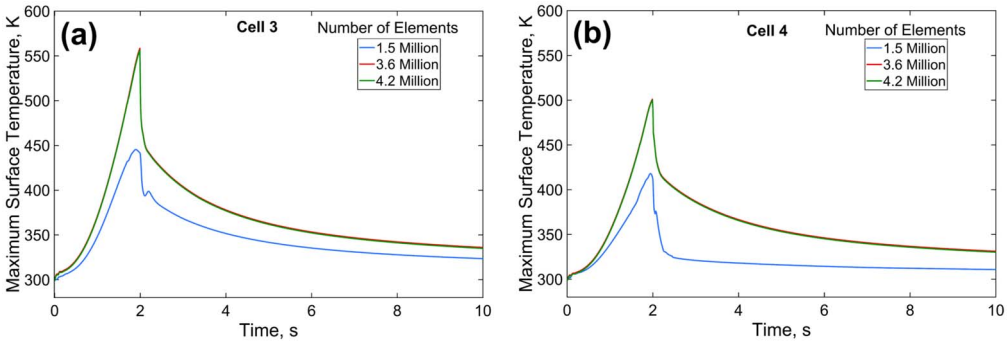

Figure 3. Simulation results to establish grid independence: Maximum surface temperature as a function of time for (a) Cell 3 and (b) Cell 4. Problem parameters include 5 mm overhead gap, 4 mm cell-to-cell gap, 2 s venting time and 7mm^2 vent placed at center of top surface of Cell 1.

Figure 2 shows that the vent temperature continues to increase throughout the venting process, whereas the vent velocity reaches a peak and then comes down. This trend directly results from the experimental measurements of stagnation pressure[27] underlying these calculations, which show that stagnation pressure decreases with time. Since the stagnation pressure is directly proportional to the Mach number, as seen in Eq. 8, this may result in reduction in speed after much of the trigger cell has emptied out. On the other hand, decrease in vent velocity causes vent temperature to increase as seen in Eq. 10. This inverse proportionality results from the conversion of pressure energy into intermolecular thermal energy.

Meshing and other simulation details.—A 3D polyhedral meshing technique is used in all simulations due to its high resolution, smaller residual values and lower meshing time compared to other meshing techniques. Polyhedral meshing increases number of neighboring simulation cells, which, in turn, improves gradient approximation and reduces probability of errors. Global mesh controls allow automatic calculation of global element size based on smallest geometric entity. The smallest element length used is 10^{-5} m, and advanced sizing functions are used for resolving regions with curvature and proximity. Other mesh parameters include a growth rate of 1.1 and squish index of 0.28. A total of 7.2 million elements are used in each simulation. Mesh independence of results is established and is discussed in a subsequent section.

Venting of hot ejecta lasts for first two seconds of the simulation requiring extremely small time stepping to meet the convergence criteria. Hence, 0.01 millisecond fixed time stepping and 0.001 relative tolerance limit are used during the venting phase of the simulation. For rest of the simulation, an extremely fine timestep is not needed since the high speed venting process has stopped. In this regime, a 1 millisecond timestep is used in order to minimize computation time while keeping residuals within tolerance. Simulation is stopped at 10 s, since by this time, the cells have either cooled down substantially or onset of thermal runaway has occurred. A comprehensive mesh sensitivity analysis is performed prior to actual simulations in order to determine the required spatial discretization to obtain grid-independent results.

Results and Discussion

A summary of goals, parameters and key conclusions of each simulation described in this section is summarized in Table II. Each simulation is labeled, in order to enable cross-referencing between the summary in Table II and detailed discussion below.

The establishment of grid independence of the simulation results is discussed first. A baseline simulation (Simulation A) comprising 25 cells is carried out, as shown in Fig. 1. In this simulation, the cell-to-cell gap and overhead gap are 4 mm and 5 mm, respectively, and venting occurs for 2 s duration from a 7 mm^2 hole at the top of the trigger cell located at a corner of the geometry. As discussed in the previous section, Arrhenius heat generation is considered in all cells, except the trigger cell, to model thermal runaway if a certain threshold temperature is exceeded. Temperature and velocity fields are computed as functions of time using the methodology discussed in the previous section. The maximum surface temperature of cells 3 and 4 are plotted in Figs. 3a and 3b, respectively, for three different grid sizes. When the number of elements is increased from 1.5 million to 3.6 million, both Figs. 3a and 3b show significant change in the predicted temperature. However, increasing further to 4.2 million elements changes the resulting temperature distribution only by 3%. This establishes grid independence at 3.6 million elements, which is the grid size used for all the simulations discussed in the remainder of this work.

In order to understand the nature of thermal and fluid transport occurring in this system, color plots of the temperature and velocity fields in the interstitial air around the cells are plotted at different times for a simulation with the cell-to-cell gap of 1 mm in Figs. 4a and 4b, respectively. Similar plots for the cell-to-cell gap of 4 mm are presented in Fig. 5. In these plots, the trigger cell is shown in dark gray color on the left end of the cross-section, and the vent location at the top surface of the trigger cell is also indicated with a red arrow. The overhead gap is 1 mm in each case. Both temperature and velocity color plots indicate that the thermal and fluid fields are rapidly established following the start of venting, with the vent gas advancing outwards over time. Some retraction in the gas front is observed towards the end of venting, which may be due to the reduction in vent speed, as shown in Fig. 2b. More ejecta is found to settle in the gap between cells when the cell-to-cell gap is 4 mm, which is likely due to the lower resistance to flow into these gaps. Specifically, there is a large temperature rise in the gap between the trigger cell and cell 2. While this increases the risk of thermal runaway in cell 2, it may reduce the risk to other cells, which may be desirable for preventing propagation. Note that increasing the cell-to-cell gap also increases the distance that the vent gas must travel to reach other cells. However, this is unlikely to influence the likelihood of propagation much due to the very high speed at which vent gas is ejected. Instead, the propensity of the vent gas to get trapped between trigger cell and cell 2 when the cell-to-cell gap is increased is likely to be a more influential phenomena in determining whether thermal runaway propagates or not.

For a more detailed investigation of the influence of cell-to-cell gap on thermal runaway propagation, peak temperatures on the surfaces of various cells are plotted as functions of time for cell-to-cell gaps of 1 mm and 4 mm in Figs. 6 and 7, respectively (Simulations B and C). Other relevant parameters used in both simulations include an overhead gap of 1 mm, vent time of 2 s, and 7 mm^2 vent located on top surface of the trigger cell. Temperature color plots at four different times are also shown in Figs. 6 and 7. Note that these Figures plot the maximum surface temperature. The corresponding color plots indicate that the peak temperature is reached only in a small area of the cell surface, and most of the cell remains quite cold within the short simulation period.

Figure 6 shows that when the cell-to-cell gap is 1 mm, the propagation of thermal runaway is quite extensive. Cells 2, 7, 8, 9,

Table II. Summary of parameters and results from all simulations presented in this work.

Simulation #	To Study	Figure #	Geometrical Parameters				Key Conclusions
			Vent Location	Cell-to-Cell Gap (mm)	Overhead Gap (mm)	External Opening Location	
A	Grid Independence	3a, 3b	Top Surface, Cell 1	4	5	—	3.6 M elements are sufficient for 25-cell 18650 Li-ion battery pack.
B	Effect of Cell-to-Cell gap	6	Top Surface, Cell 1	1	1	—	Increasing cell-to-cell gap reduces probability of thermal runaway propagation.
C		7		4			
D	Effect of Overhead Space	9	Top Surface, Cell 1	1	5	—	Increasing overhead gap prevents thermal runaway propagation.
E		10		4			
F	Effect of Vent Location	11	Curved Surface, Cell 1	1	1	—	Cell rupture from the side-wall may accelerate thermal runaway propagation due to direct impingement on neighboring cells.
G		12		4			
H	Effect of External Opening	13	Top Surface, Cell 1	1	1	Above Cell 13	Location of the external opening influences flow distribution, and hence, the propagation of thermal runaway.

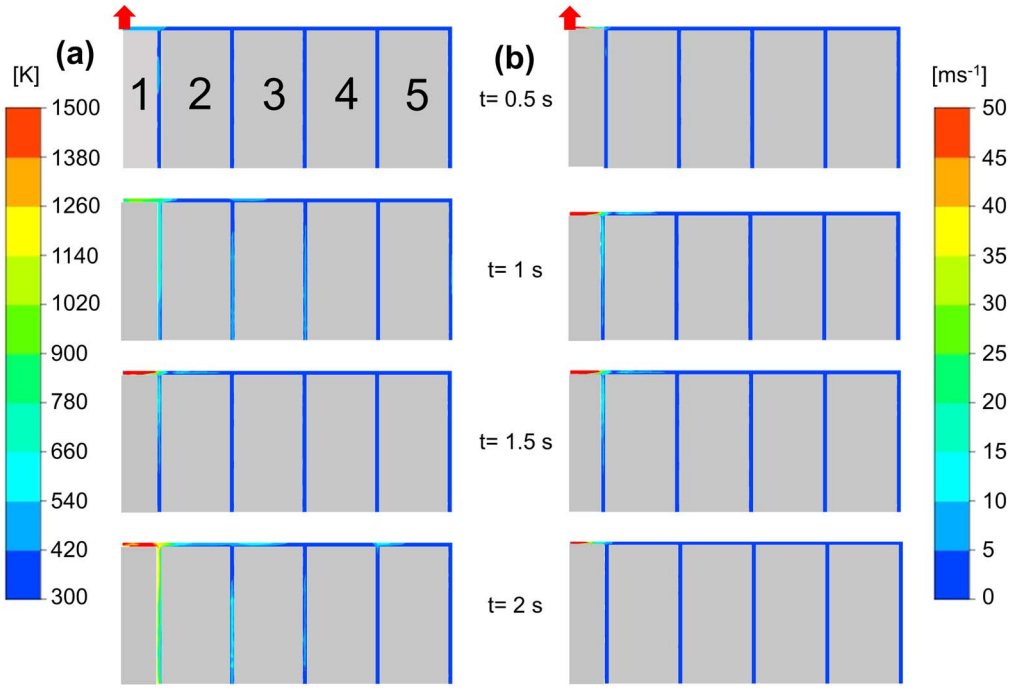

Figure 4. Color plots in the XZ plane showing evolution of the (a) temperature and (b) velocity fields at various times for 1 mm overhead gap and 1 mm cell-to-cell gap. The vent hole is located at the center of the top surface of trigger cell.

13 and 14 all reach very high temperatures within the 2 s vent duration. For cells 2, 7 and 8, the thermal excursion is sufficiently extensive that a very high temperature is sustained even after venting stops. In this case, sufficient volume of the cell has overheated, so that the heat generated by decomposition reactions is enough to initiate substantial self-heating in the cell even after venting stops. In contrast, even though the maximum surface temperature of cells 9, 13 and 14 also becomes high, the volume of the cell impacted is smaller, which results in unsustained thermal runaway and reduction in peak temperature once the venting stops.

In comparison to the 1 mm cell-to-cell scenario presented in Fig. 6, Fig. 7 shows a very different nature of thermal runaway propagation when the cell-to-cell gap is 4 mm. In this case, only cell 2 experiences sustained thermal runaway. As the vent gas spreads out from the trigger cell, the flow resistance offered by the gap between trigger cell and cell 2 relative to the flow resistance offered by the overhead gap plays a key role in determining whether the vent gas spreads further outwards or mostly gets lodged in the gap. When the cell-to-cell gap is only 1 mm, there is large resistance to flow into the gap between cells, due to which, the hot vent gas flows preferentially in the overhead

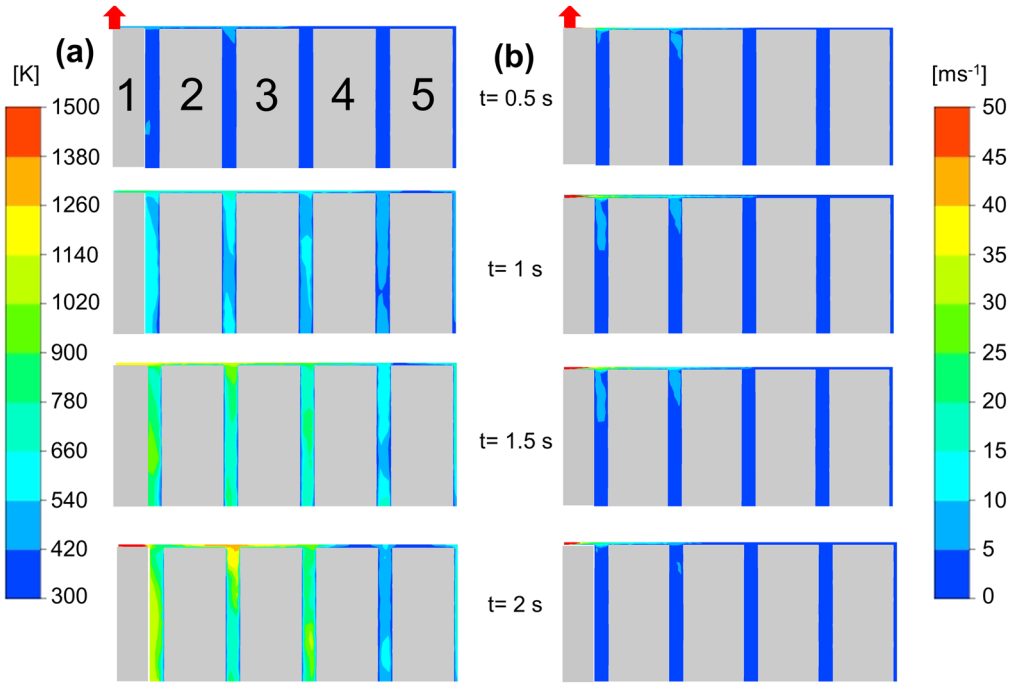

Figure 5. Color plots in the XZ plane showing evolution of the (a) temperature and (b) velocity fields at various times for 1 mm overhead gap and 4 mm cell-to-cell gap. The vent hole is located at the center of the top surface of trigger cell.

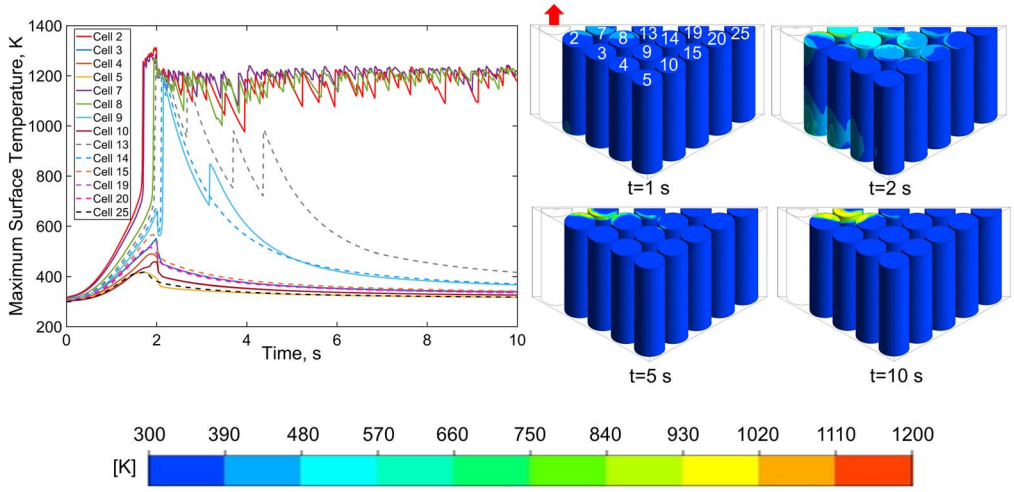

Figure 6. Effect of Cell-to-cell gap: Temperature plots for 1 mm cell-to-cell gap. Other parameters include 1 mm overhead gap, 2 s venting time and 7 mm^2 vent placed at center of top surface of the trigger cell.

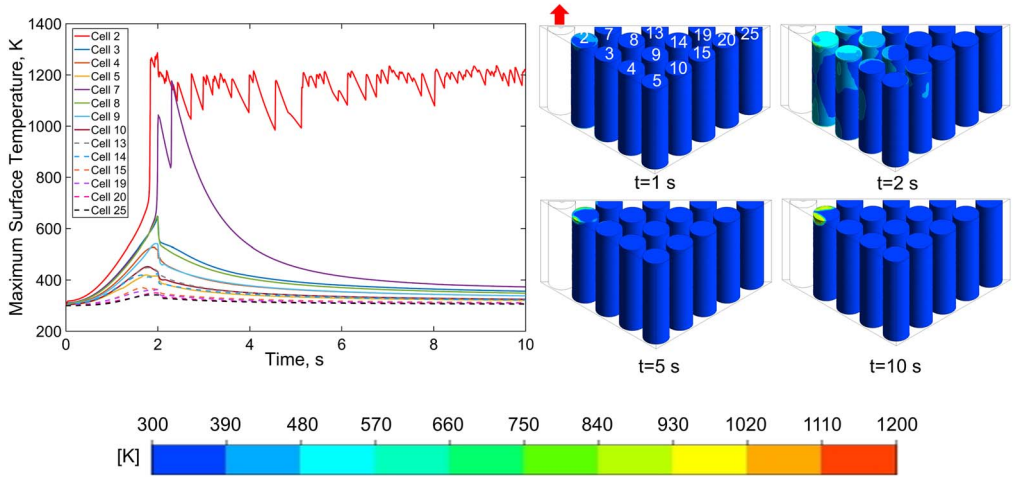

Figure 7. Effect of cell-to-cell gap: Temperature plots for 4 mm cell-to-cell gap. Other parameters include 1 mm overhead gap, 2 s venting time and 7 mm^2 vent placed at center of top surface of the trigger cell.

region, causing extensive propagation of thermal runaway as seen in Fig. 6. On the other hand, when the cell-to-cell gap is relatively larger, for example 4 mm, there is much lower resistance to flow into the gap between cells, due to which, more hot vent gas flows in the gap between cells, thereby limiting the extent of outward propagation. In this case, most of the thermal impact of the vent gas is absorbed by cell 2, which undergoes thermal runaway, but partly protects other cells from thermal runaway.

The reduced propensity of thermal runaway propagation at large cell-to-cell gap observed in Fig. 7 is consistent with past experimental measurements that suggest an inverse relationship between cell-to-cell gap and thermal runaway propagation intensity. For example, past experimental work suggests a spacing of at least 2 mm between 18650 cells in a module to prevent thermal runaway propagation.[8] In a separate work, it was shown that 4 mm horizontal spacing and 8 mm vertical spacing is required to suppress thermal runaway propagation in 18650 battery pack.[44] Both observations are qualitatively consistent with the conclusions of the present work.

Note that the only venting considered in this work is from the trigger cell. Secondary venting from other cells that may undergo thermal runaway later is not modeled in this work.

Figure 7 shows that maximum surface temperature on cell 7 is very high during the venting period, but once venting stops, this does not lead to sustained heating typical of thermal runaway. This is because only a very small region of the cell overheats, which is not sufficient to trigger and sustain thermal runaway once the heat input from the venting gases stops. Since the hot vent gas flow is similar to a jet, temperature rise due to hot vent gas is a highly directed phenomenon—there is large temperature rise where the vent gas jet impinges directly, with relatively minor impact elsewhere. This is the reason why there is no sustained thermal runaway in several cells despite a very high value of the maximum temperature rise seen in Figs. 6 and 7. This is confirmed in Fig. 8, which presents temperature color plots of two contrasting cells for the 1 mm cell-to-cell gap case. Even though cells 2 and 14 both show very high maximum temperature in Fig. 6, a temperature color plot of the two cells shown in Fig. 8 indicates that the large temperature rise in cell 2 is observed over a much larger surface area than cell 14, which is why cell 14 cools down to ambient after the gas venting stops, whereas cell 2, having absorbed sufficient thermal energy, enters thermal runaway sustained by the heat from its own exothermic reactions.

Figure 8 also shows that in many cases, the surface area impacted is very small, even though the local temperature rise is large. This is the reason why in some cases, heat from the hot spot is rapidly absorbed by the larger and cooler portions of the cell, leading to a sudden drop in temperature after venting stops, as observed for several cells.

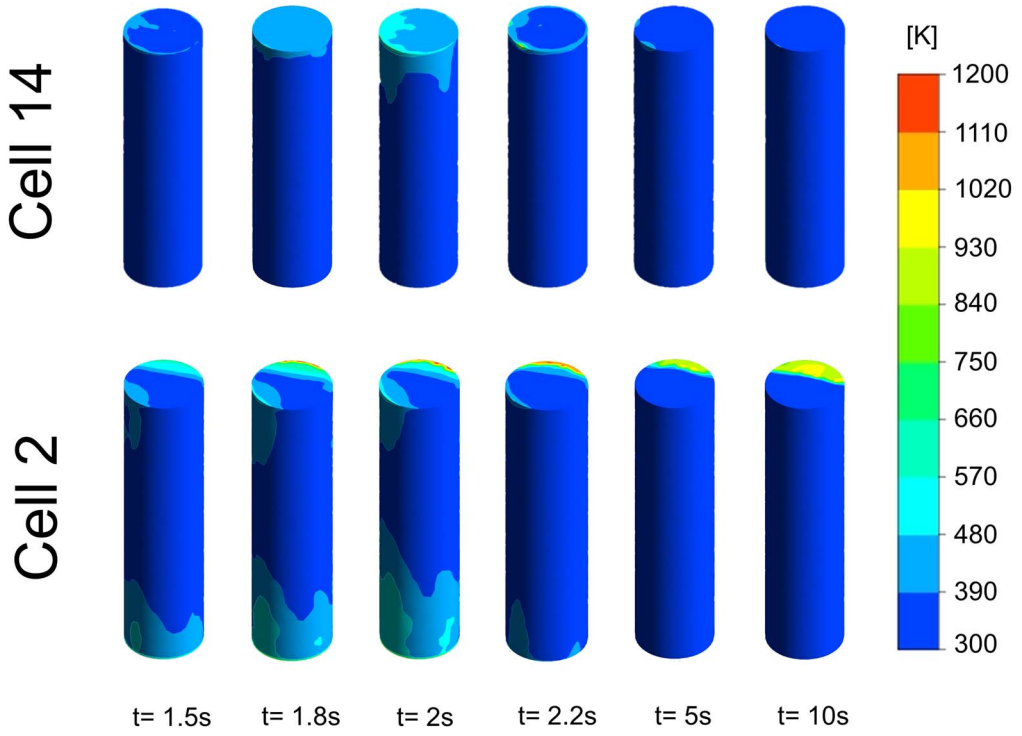

Figure 8. Temperature plots cell 14 and cell 2 for 1 mm cell-to-cell gap. Other parameters include 1 mm overhead gap, 2 s venting time and 7 mm^2 vent placed at center of top surface of the trigger cell.

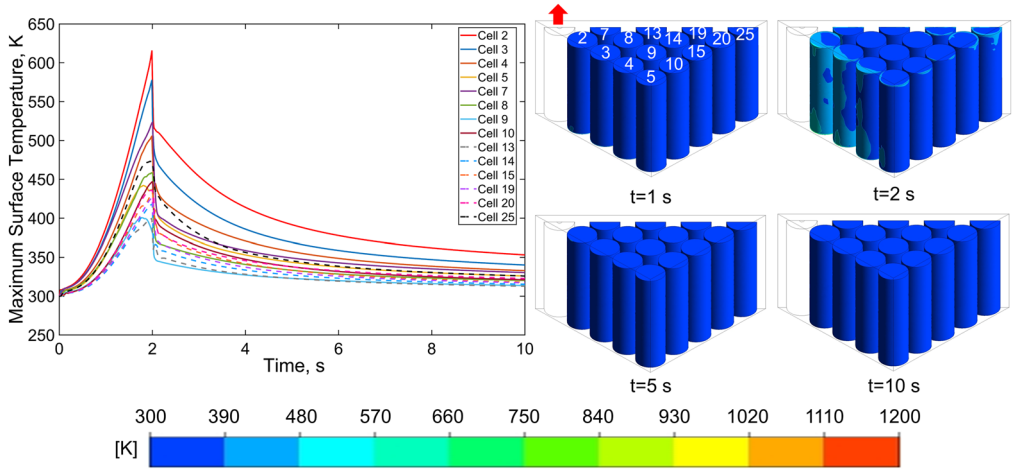

Figure 9. Effect of overhead space: Temperature plots for 5 mm overhead gap, 2 s venting time and 7 mm^2 vent placed at center of top surface of the trigger cell for 1 mm cell-cell gap.

The effect of the overhead gap is investigated next. Similar to the cell-to-cell gap, the overhead gap may play a key role in determining the nature of vent gas flow, and thus the propagation of thermal runaway by changing the volume and flow resistance offered by the overhead space relative to the flow resistance offered by the gap between the cells. The scenarios in Figs. 6 and 7, presented earlier, correspond to an overhead gap of 1 mm. In order to investigate the impact of increasing the overhead gap, simulations are carried out at an overhead gap of 5 mm. Two different cell-to-cell gaps of 1 mm and 4 mm are simulated, and shown in Figs. 9 and 10 (Simulations D and E), respectively. In both cases, the volume of the overhead gap is large enough that the heat carried by the vent gases is sufficiently absorbed by air in the overhead gap without significant rise in temperature in any of the cells. At an overhead gap of 5 mm, therefore, there is no significant propagation of thermal runaway, even when the cell-to-cell gap is relatively small. This suggests that it may be possible to safely store cells in a dense configuration by increasing the overhead gap.

The physical location and orientation of the vent hole on the trigger cell is also expected to play a key role in thermal runaway propagation since it governs the direction of the vent gas jet. When the vent hole is located on the top surface, the jet is not directly targeted towards any of the neighboring cells. However, if the trigger cell ruptures on the side surface, leading to venting from the side, then the hot vent gas may impinge directly on one of the neighboring cells, making it more likely for thermal runaway to propagate. A set of simulations are carried out with the vent hole located on the curved surface of the trigger cell in order to compare with prior results in which the vent hole was located on the top surface. In this case, the vent hole of the same size as before is located on the curved

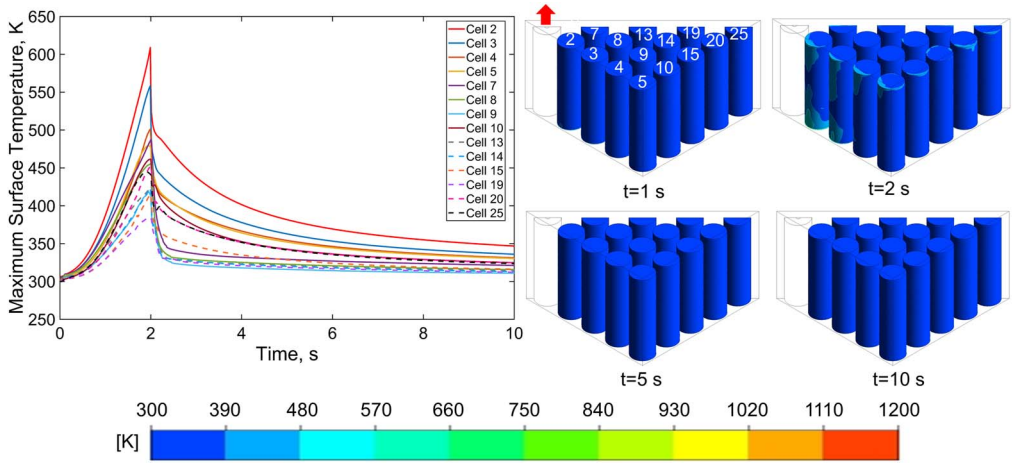

Figure 10. Effect of overhead space: Temperature plots for 5 mm overhead gap, 2 s venting time and 7 mm^2 vent placed at center of top surface of the trigger cell for 4 mm cell-cell gap.

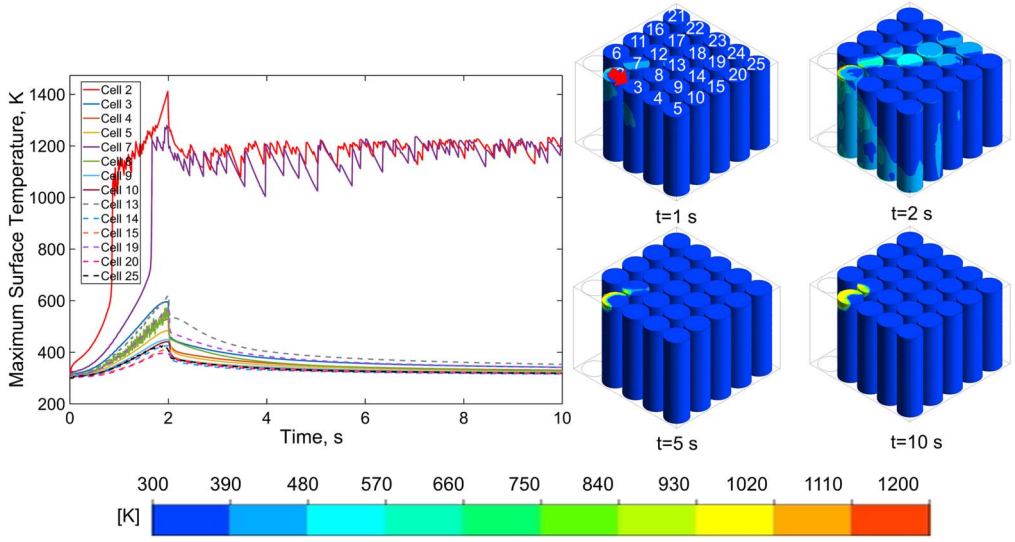

Figure 11. Effect of location of vent: Temperature plots for 1 mm overhead gap, 2 s venting time and 7 mm^2 vent placed at 62.5 mm height on curved surface of the trigger cell facing cell 2 for 1 mm cell-cell gap.

surface, 2.5 mm below the top surface of the cell and directed towards cell 2. Two cases of cell-to-cell gap of 1 mm and 4 mm are simulated. Peak surface temperatures on various cells as functions of time are presented for these two cases in Figs. 11 and 12 (Simulations F and G), respectively. Results show that in the first case (Fig. 11), due to the very small distance between the vent and neighboring cells, the narrow venting jet impinges directly on the immediate neighbors, cells 2 and 7, and most of the vented energy is absorbed by these cells. On the other hand, when the cell-to-cell gap is larger (Fig. 12), the venting jet becomes more distributed before reaching the neighboring cells, resulting in impingement on a greater number of cells. As a result, there is greater propagation and a larger number of impacted cells, as shown in Fig. 12. The deflected trajectories of ejecta upon impingement in cells in the battery pack can be visualized through color plots shown in Figs. 11 and 12.

Finally, simulations are carried out to understand the impact of placing an external opening on the top of the battery pack to safely remove the vent gases and prevent thermal runaway propagation. Normally, such an external opening would open to ambient pressure, and therefore, attract the vent gases that escape from the vent hole at a much higher pressure. While the exit of vent gas is, in principle, desirable, it is important to carefully choose the location of the external opening because the external opening can create an undesirable flow pattern of the vent gas within the battery pack, which may cause propagation of thermal runaway. To investigate this in detail, two simulations are carried out with different locations of the external opening on top of the battery pack. In the first case, the opening is located directly above the location of the vent hole on the trigger cell. In the second case, the opening is located above the center of cell 13. As expected, when the external opening hole is located directly above the vent hole, the venting gases flow upwards and directly exit the battery pack through the external opening, resulting in no temperature rise in the neighboring cell at all. Due to the trivial nature of this case, temperature color plots are not shown. Figure 13 (Simulation H) shows the predicted temperature field when the opening is located above the center of cell 13. In this case, a flow pattern of vent gases flowing from the high-pressure region just above the trigger cell to the low pressure opening above cell 13 is created. This inadvertently exposes several other cells to high temperature and causes thermal propagation clearly seen in the color plots and temperature plots in Fig. 13, both of which show propagation of thermal runaway to several cells in the pathway between trigger cell and cell 13.

The scenario discussed above is, of course, a best-case scenario, in which the location of the trigger cell and the vent hole is assumed

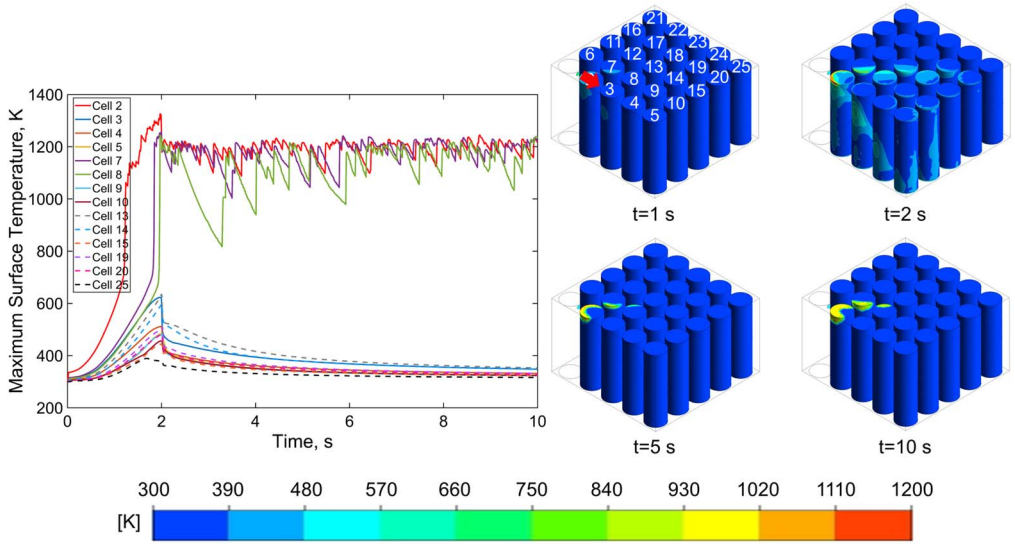

Figure 12. Effect of location of vent: Temperature plots for 1 mm overhead gap, 2 s venting time and 7 mm^2 vent placed at 62.5 mm height on curved surface of the trigger cell facing cell 2 for 4 mm cell-cell gap.

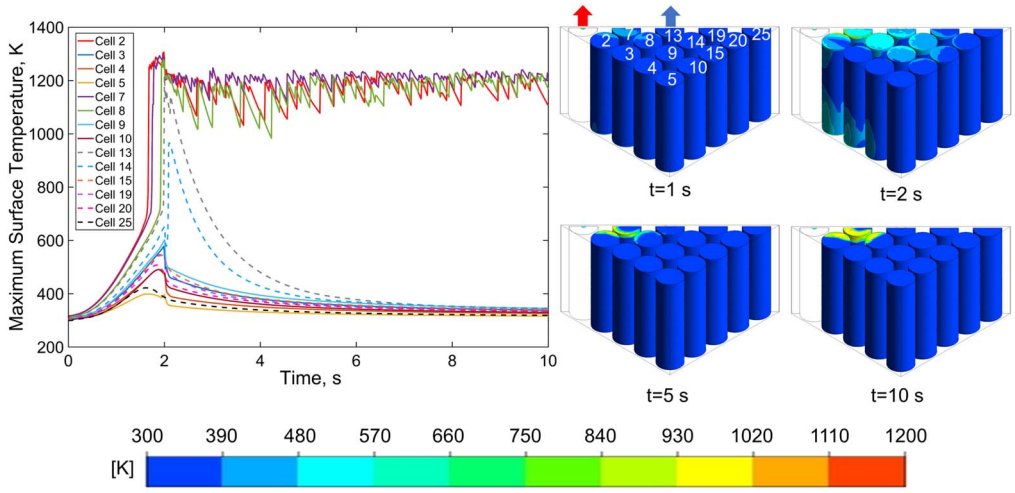

Figure 13. Effect of external opening: Temperature plots for 1mm cell-to-cell gap, 1 mm overhead gap, 2 s venting time and 7 mm^2 vent placed at center of top surface of the trigger cell. The external opening is located above cell 13.

to be known in advance. Ideally, the external opening would be placed directly above the trigger cell. However, in reality, which cell will fail, and the vent location on the cell may not be known in advance. Therefore, it is not straightforward to choose the location of the external opening. Of course, placing an external opening above every cell would greatly help suppress thermal runaway propagation, but doing so may be prohibitively expensive. It may be possible to optimize the number of vents and their locations to minimize the propagation of thermal runaway in the battery pack regardless of the location of the trigger cell, while keeping the cost of building such a pack reasonably low.

Conclusions

The simulation of venting gas ejecting from a ruptured Li-ion cell in a battery pack presents several technical difficulties. The vent gas flow is supersonic and turbulent. The resulting conservation equations are highly non-linear. Moreover, the key boundary conditions including temperature and flowrate at the vent are not well known. This work addresses these challenges by first estimating the vent gas temperature and flowrate as it exits the trigger cell based on isentropic flow assumption. Further, a multi-physics simulation framework is developed to predict the resulting thermal and fluid flow fields in the battery pack. This helps predict how the vent gas transfers thermal energy to neighboring cells, which may cause propagation of thermal runaway. The impact of geometrical parameters such as cell-to-cell gap, overhead gap as well as the location of the vent hole (top surface vs side wall) on thermal runaway propagation predicted by this model may be of much practical interest.

Note that the results presented in this work are based on previously-reported stagnation pressure measurements underlying the calculation of temperature and flow boundary conditions, which may vary significantly from one abuse condition to the other. The impact of cell capacity and SOC is also not captured in the present model. Another limitation of the present work is that only venting from the trigger cell is considered. Secondary venting events that may occur as neighboring cell get impacted are not modeled here. Finally, the presence of solid particles in the vent gas flow has been ignored. Measurements and modeling of solid particles in the flow, while quite challenging, is a potential direction for future work.

This work addresses a key gap in the literature by developing a simulation model that predicts the spreading of venting gases in the battery pack and consequently the propagation of thermal runaway to neighboring cells. It is expected that design guidelines

based on such a simulation tool may be helpful for designing battery packs that can better withstand thermal runaway propagation, resulting in more reliable electrochemical energy conversion and storage systems.

Acknowledgments

This material is based upon work supported by CAREER Award No. CBET-1554183 from the National Science Foundation.

ORCID

Ankur Jain https://orcid.org/0000-0001-5573-0674

References

1. T. M. Bandhauer, S. Garimella, and T. F. Fuller, *J. Electrochem. Soc.*, **158**, R1 (2011).
2. Q. Wang, P. Ping, X. Zhao, G. Chu, J. Sun, and C. Chen, *J. Power Sources*, **208**, 210 (2012).
3. A. Melcher, C. Ziebert, M. Rohde, and H. J. Seifert, *Energies*, **9**, 292 (2016).
4. M. N. Richard and J. R. Dahn, *J. Power Sources,*, **79**, 135 (1999).
5. E. P. Roth and D. H. Doughty, *J. Power Sources,*, **128**, 308 (2004).
6. S. Santhanagopalan, P. Ramadass, and J. Z. Zhang, *J. Power Sources,*, **194**, 550 (2009).
7. X. Feng, M. Fang, X. He, M. Ouyang, L. Lu, H. Wang, and M. Zhang, *J. Power Sources,*, **255**, 294 (2014).
8. C. F. Lopez, J. A. Jeevarajan, and P. P. Mukherjee, *J. Electrochem. Soc.*, **162**, A1905 (2015).
9. D. Mishra and A. Jain, *J. Electrochem. Soc.*, **168**, 20504 (2021).
10. Q. Li, C. Yang, S. Santhanagopalan, K. Smith, J. Lamb, L. A. Steele, and L. Torres-Castro, *J. Power Sources*, **429**, 80 (2019).
11. L. Torres-Castro, A. Kurzawski, J. Hewson, and J. Lamb, *J. Electrochem. Soc.*, **167**, 090515 (2020).
12. K. S. Kshetrimayum, Y.-G. Yoon, H.-R. Gye, and C.-J. Lee, *Appl. Therm. Eng.*, **159**, 113797 (2019).
13. S. Wilke, B. Schweitzer, S. Khateeb, and S. Al-Hallaj, *J. Power Sources,*, **340**, 51 (2017).
14. Z. An, K. Shah, L. Jia, and Y. Ma, *Appl. Therm. Eng.*, **160**, 113960 (2019).
15. T. Liu, C. Tao, and X. Wang, *Appl. Energy*, **267**, 115087 (2020).
16. X. Yang et al., *Fire Technol.*, **56**, 2579 (2020).
17. L. Huang, Z. Zhang, Z. Wang, L. Zhang, X. Zhu, and D. D. Dorrell, *J. Energy Storage*, **25**, 100811 (2019).
18. J. Lamb, C. J. Orendorff, L. A. M. Steele, and S. W. Spangler, *J. Power Sources*, **283**, 517 (2015).
19. J. K. Ostanek, W. Li, P. P. Mukherjee, K. R. Crompton, and C. Hacker, *Appl. Energy*, **268**, 114972 (2020).
20. P. T. Coman, S. Mátéfi-Tempfli, C. T. Veje, and R. E. White, *J. Electrochem. Soc.*, **164**, A1858 (2017).
21. P. J. Bugryniec, D. J. N. Davidson, and D. S. F. Brown, *J. Power Sources,*, **474**, 228396 (2020).
22. D. Sturk, L. Rosell, P. Blomqvist, and A. A. Tidblad, *Batteries*, **5**, 1 (2019).
23. L. Yuan, T. Dubaniewicz, I. Zlochower, R. Thomas, and N. Rayyan, *Process Saf. Environ. Prot.*, **144**, 186 (2020).
24. G. Gachot, S. Grugeon, I. Jimenez-Gordon, G. G. Esheta, S. Boyanov, A. Lecocq, G. Marlair, S. Pilard, and S. Laruelle, *Anal. Methods*, **6**, 6120 (2014).
25. A. W. Golubkov, R. Planteu, G. Voitic, H. Wiltsche, C. Stangl, G. Fauler, A. Thaler, and V. Hacker, *RSC Adv.*, **5**, 57171 (2015).
26. J. Kim, A. Mallarapu, D. P. Finegan, and S. Santhanagopalan, *J. Power Sources*, **489**, 229496 (2021).
27. F. Austin Mier, M. J. Hargather, and S. R. Ferreira, *J. Fluids Eng. Trans. ASME,*, **141**, 1 (2019).
28. W. Li, K. R. Crompton, C. Hacker, and J. K. Ostanek, *J. Energy Storage*, **32**, 101890 (2020).
29. L. Kong, X. Hu, G. Gui, Y. Su, and M. Pecht, *Fire Technol.*, **56**, 2565 (2020).
30. B. A. Egan and J. R. Mahoney, *J. Appl. Meteorol. Climatol.*, **11**, 312 (1972).
31. C. Jia, K. Shing, and Y. C. Yortsos, *Water Resour. Res.*, **35**, 3239 (1999).
32. S. R. Allmaras and F. T. Johnson, *Seventh International Conference on Computational Fluid Dynamics (ICCFD7)*, Big Island, HI, p. 1 (2012).
33. S. Deck, P. Duveau, P. D'Espiney, and P. Guillen, *Aerosp. Sci. Technol.*, **6**, 171 (2002).
34. M. Parhizi, M. B. Ahmed, and A. Jain, *J. Power Sources,*, **370**, 27 (2017).
35. G. H. Kim, A. Pesaran, and R. Spotnitz, *J. Power Sources,*, **170**, 476 (2007).
36. S. J. Drake, D. A. Wetz, J. K. Ostanek, S. P. Miller, J. M. Heinzel, and A. Jain, *J. Power Sources,*, **252**, 298 (2014).
37. T. S. Bowling and J. A. Terr, *Phys.*, **56**, 539 (1994).
38. T. Walker, S. C. Xue, and G. W. Barton, *J. Heat Transfer*, **132**, 1 (2010).
39. P. H. Oosthuizen and W. E. Carscallen, *Introduction to Compressible Fluid Flow* (CRC press, Boca Raton, FL) (2013).
40. W. Li, H. Wang, Y. Zhang, and M. Ouyang, *J. Energy Storage*, **24**, 100775 (2019).
41. A. W. Golubkov, D. Fuchs, J. Wagner, H. Wiltsche, C. Stangl, G. Fauler, G. Voitic, A. Thaler, and V. Hacker, *RSC Adv.*, **4**, 3633 (2014).
42. I. H. Bell, S. Quoilin, J. Wronski, and V. Lemort, ASME ORC 2nd International Seminar on ORC Power Systems (2013), http://www.coolprop.org/.
43. F. M. White and I. Corfield, *Viscous Fluid Flow* (McGraw-Hill, New York, NY) (2006).
44. Z. Wang, N. Mao, and F. Jiang, *J. Therm. Anal. Calorim.*, **140**, 2849 (2020).